

A High Performance Voice Coil Actuator for Optomechatronic Applications

Dion Hicks

Faculty of Engineering and Applied Science,
Memorial University of Newfoundland,
St. John's, NL A1C 5S7, Canada
e-mail: dionh@mun.ca

Taufiq Rahman

Agile Sensors Technology Inc.,
St. John's, NL A1A 3W8, Canada
e-mail: me.trahman@gmail.com

Nicholas Krouglicof

School of Sustainable Design Engineering,
University of Prince Edward Island,
Charlottetown, PE C1A 4P3, Canada
e-mail: krouglicof@upei.ca

Voice coil actuators (VCAs) are simple electro-mechanical devices, which are capable of generating linear motion in response to an electrical input. The generic cylindrical design of commercially available actuators imposes a large variety of limitations on the end user. The most prominent is the requirement to design and fit extra components to the actuator in order to increase functionality. To solve this issue, a novel voice coil actuator was created, which reconfigures the standard cylindrical design with one of a rectangular structure. The novel actuator incorporates planar magnets in a modified Halbach array configuration to ensure compactness and an exceptionally intense, uniform magnetic field. The moving coil is substituted with a printed circuit board (PCB) encompassing numerous current conducting traces. The board contains a miniature linear rail and bearing system, unified drive electronics, and highly adaptive position feedback circuitry resulting in a compact, highly dynamic and accurate device. In pursuit of optomechatronic applications, two distinct parallel kinematic mechanisms (PKMs) were developed to utilize the high dynamics and accuracy of the novel actuator. These devices were configured to function in only rotational degrees-of-freedom (DOF) and because of their underlying kinematic structures can be referred to as parallel orientation manipulators (POMs). In particular, two structures were defined, 2-PSS/U and 3-PSS/S, in order to constrain their payloads to two and three degrees of rotational freedom, respectively. The resultant manipulators are highly dynamic, precise and fulfill size, weight, and power requirements for many applications such as sense and avoidance and visual tracking. [DOI: 10.1115/1.4035879]

1 Introduction

Voice coil actuators (VCAs) are noncommutative, simple electro-mechanical mechanisms which generate motion in response to an electrical input. Generally, they consist of a current conducting coil located inside of a strong magnetic field generated by a stationary permanent magnet(s) [1,2]. The force produced by VCAs is known as the Laplace (Lorentz) force and is equated to be $F = BLI$, where B is the magnetic field or flux density, L is the conductor length, and I is the coil current [3,4].

Though many off-the-shelf linear actuators are commercially available [5,6] and are mentioned throughout the literature [7,8], their generic cylindrical design facilitates a great deal of limitations when trying to meet the special requirements of many optomechatronic applications. The greatest drawback is that it is the responsibility of the end user to fit the actuator with supplementary components in order to increase functionality. These components are inclusive to linear motion guidance systems, position feedback devices, and current driving electronics. The addition of multiple devices not only reduces the reliability of the mechanism but also makes packaging and system minimization problematic.

To this end, a novel VCA was developed which replaces the standard cylindrical design with one of a rectangular nature. While instances of this architecture exist in literature [9,10] and industry [11–13], an innovative approach was undertaken to increase the capabilities of the actuator by replacing many of the essential components found in these devices. However, directly comparing linear actuators is difficult as many characteristics of the mechanisms can be used to evaluate their overall validity. These include size, moving mass, overall weight, stroke length,

power consumption, velocity, acceleration, and its time constant. However, one actuator discovered in industry [14] is very similar to the proposed design, with some contrasting features, which will be highlighted in Sec. 2.2.

The proposed rendition was accomplished through four fundamental changes in the traditional cylindrical design. The first of which is the use of planar magnets in modified Halbach array [15] configuration. While Halbach arrays exist in literature [9,10], they are not typically implemented in a completed mechanism. Nonetheless, these provide not only compactness but also an exceptionally uniform, internally concentrated magnetic field [16]. Second, to minimize the gap between the Halbach arrays, thus increasing field strength, the traditional moving mass of the coil is replaced with that of a slim, light-weight printed circuit board (PCB) containing numerous current conducting traces. This can be considered the most unique innovation of the proposed actuator as it promotes a compact, lightweight moving mass resulting in high dynamics. It also allows for the incorporation of a guidance system, integrated drive and position sensing electronics and the PCB can be manufactured with ease and repeatability. These characteristics are generally hard to replicate on traditional designs. Third, a feedback system was created by way of a position sensitive detector (PSD), a p-i-n silicon photodetector consisting of multiple electrodes on an optically transparent, uniform resistive surface [17]. This sensor, a laser diode, and a highly adaptive signal conditioning circuit were incorporated into the VCA design to ensure noncontact position feedback, resulting in extremely precise actuation. Note, feedback devices are not generally included with actuators and when present, consist of linear encoders [12,14]. Taking advantage of the coil's geometry, miniature linear rails and bearings were added to guarantee the smooth motion of the actuator. Finally, not only are many of the subsystems innovative for the use in VCA creation, but the conglomeration of all systems forms the novelty of the proposed design.

Manuscript received July 25, 2016; final manuscript received January 11, 2017; published online May 23, 2017. Assoc. Editor: Jun Ueda.

An application that can utilize the unprecedented speed and accuracy of the novel VCA is a system known as a parallel kinematic mechanism (PKM). These devices allow a moving platform to be manipulated in the same fashion as a freely suspended body. Its translational and rotational degrees-of-freedom (DOF) are equivalent to the number of nonredundant linear actuators employed. There are a variety of PKM configurations that provide rotation and translation [18–20]; however, in many optomechatronic applications, translational displacement is unnecessary. When restricting the platform to rotational motion only, a PKM can be more accurately referred to as a parallel orientation manipulator (POM) [21]. While there are many different POM structures to consider, the 3-PSS/S (3DOF) [22] and the 2-PSS/U (2DOF) [23] were developed in order to pursue optomechatronic applications with strict criteria. These include speed, accuracy, reliability and size, weight, and power (SWaP), and especially, applications requiring the high speed manipulation of optical components such as mirrors, cameras, and laser devices [24,25].

2 Novel Voice Coil Components and Parameters

2.1 Magnetics. In comparison to conventional voice coil magnetics, a Halbach array magnetic configuration can be utilized to enhance and direct the magnetic field of a VCA [16,26]. A typical array is comprised of planar magnets of equal strength and size arranged in a linear fashion. However, these arrangements result in large variations in magnetic magnitude over small distances [27,28]. In contrast, creating an array with five neodymium magnets, of three different sizes, arranged in the correct pole orientations results in a more suitable configuration. Placing two sets of these configurations 1/4 in apart with the active area of each facing one another results in the modified array in Fig. 1.

The 1 in magnets are the primary source of the strong, uniform magnetic field experienced by the conductive traces of the PCB (discussed in Sec. 2.2). Conversely, the 1/4 in magnets direct the field between their larger counterparts, which also prevents leakage of the magnetic flux. This not only significantly increases interior field strength and uniformity but also greatly reduces the magnetism experienced by the external surroundings of the arrays. Finally, stainless steel plates were incorporated to the exterior of the array to further boost these enhancements.

Before production, modified design was configured and validated by way of the finite element method magnetics simulation software package (FEMM Version 4.2). FEMM visualizes a magnetic configuration's uniformity and field strength and is essential in the design of the modified Halbach array. Figure 2 illustrates the optimal design, which resulted in an interior field strength of approximately 7000 Gauss (0.7 Tesla) with the exterior being nearly two orders of magnitude lower.

Finally, Fig. 3 highlights the close comparison of the physical realization's interior field strength with that of the FEMM simulation. The experimental validation was accomplished by logging the normal flux density at the midgap at 0.1 in intervals with a gauss meter.

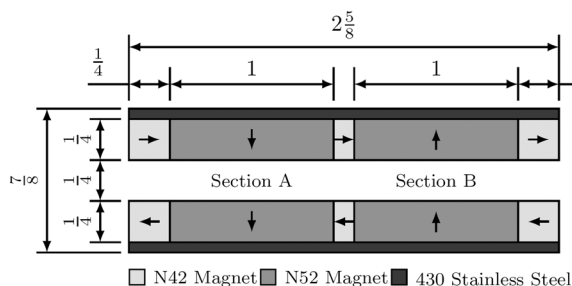


Fig. 1 Modified Halbach array with pole orientations

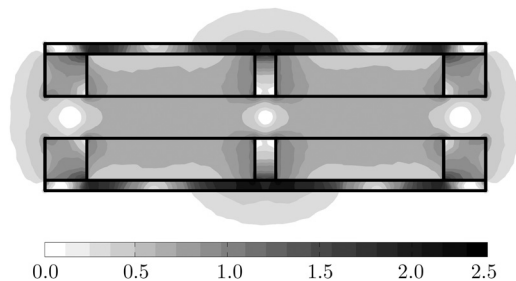


Fig. 2 FEMM simulation of the magnetic magnitude in tesla

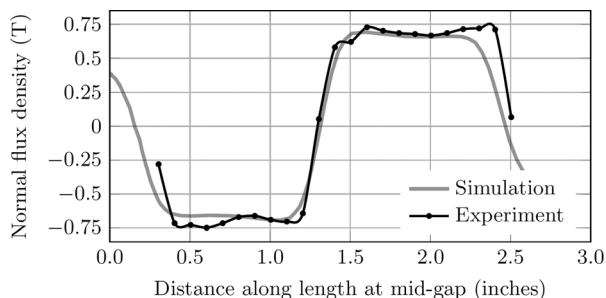


Fig. 3 Simulated and experimental results of the magnetic flux density

2.2 Voice Coil Printed Circuit Board. In contrast to conventional voice coils, the novel voice coil takes a PCB-based approach utilizing current conducting traces in place of winding. There are many benefits to a design of this nature including the ease at which they can be manufactured and increasing the traces (windings) is simple and does not drastically increase its size. Also, as it is a PCB, the surface mount electronics required to actuate and power the voice coil were integrated into its features. Finally, one of fundamental boons is its small form factor which allows the aforementioned Halbach arrays to be positioned in close proximity to one another, vastly increasing the field strength experienced by the coil's traces.

While PCBs have many benefits, they are prone to limitations such as low heat dissipation characteristics and flexing issues. However, the PCB of the proposed design exhibited little heat fluctuation during normal operations. This was concluded after exciting a number of the proposed VCAs, numerous times in different sinusoidal patterns, with short breaks of stationary positioning between each succession, in essence mirroring application usage. These experiments were uninterruptedly executed over the course of many months, resulting in millions of cycles without any failure present in either coil. Furthermore, as the VCA was not designed to actuate heavy loads, but is more inclined to be used for small-scale applications (i.e., image sensor displacement, laser pointing, etc.), flexing due to overexertion is not a concern. Additionally, while fully extended, the PCB only protrudes 34.2 mm (approximately 34%) outside of the VCA body and only 25.6 mm from the highest rail position, preventing flexing, as it is constrained by the housing and guidance system.

Since the pole orientations of the modified Halbach array cannot be altered without negatively affecting its magnetic flux, the PCB was designed to appropriately incorporate both of the regions (sections A and B) to ensure ideal Laplace force generation. To this end, spiraling current conducting traces were configured on an eight layer board. Figure 4 showcases the PCB along with the force produced when alternating currents are introduced to the system.

This particular pattern ensures that the current flows in opposite directions in sections A and B, corresponding to the alternating pole orientations found in the array. Thus, the forces generated by

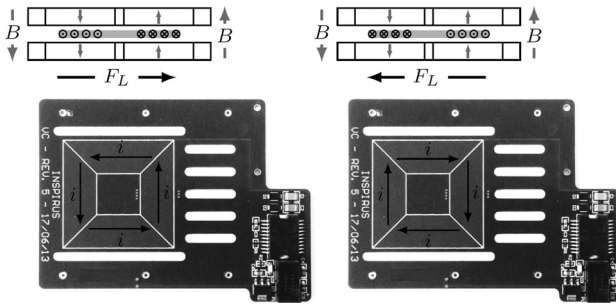


Fig. 4 Eight layer PCB with current directions and resulting force generation

each section sum together and act in the same direction, essentially doubling the force constant of the actuator. Therefore, it is imperative that neither of the coil sections cross into the opposing sections of the array; otherwise, they would negatively affect the force output. Note, the movement of the actuator is not affected by the force generated by the upper and lower traces of the coil as they terminate each other.

The fiberglass material of the PCB design is very thin in nature, typically 62 mil, while each trace on the board is a nominal 6 mil thick with 14 mil spacing between each trace; tolerances specified by manufacturing. In comparison to the four layer board of previous actuator iteration [29], this design boasts an eight layer configuration with a considerable 10.88 m of current conducting trace in a tiny area of 2.62 sq in. Of course, as described above, approximately only half of this length, 5.44 m, affects the force generated by the actuator. Since $F = BLI$, the doubling of the length of the traces effectively increased the force constant of the previous design by a factor of two. As seen in Fig. 5, the constant has now been experimentally determined to be approximately 6.9478 N/A in comparison to the previous design's 3.3 N/A. The resistivity of the coil has also been augmented, with a typical resistance of 20.44 Ω in contrast to the previous design's 8.44 Ω .

2.3 Feedback System. In comparison to bulky position measuring devices such as linear variable differential transformers (LVDTs) and linear encoders, a position sensitive detector is a more optimal choice for VCAs as it can be easily integrated into a small form factor. Also, PSDs have many advantages compared to other displacement sensors, which include high-resolution feedback, fast response time, simple operating circuits, and are noncontact in nature. To achieve an extremely accurate position sensing device, a one-dimensional (1D) PSD was used in conjunction with a vertical cavity surface emitting laser (VCSEL). In particular, the high-resolution S3932 1D PSD [30], with an active area of 12 mm, and the OPV382 diode, capable of producing a high intensity light spot of less than 200 μm in diameter, were chosen. These two devices, in conjunction with a signal conditioning circuit, provide the basis of the extremely accurate position sensing mechanism. For ease of manufacturing and design, the

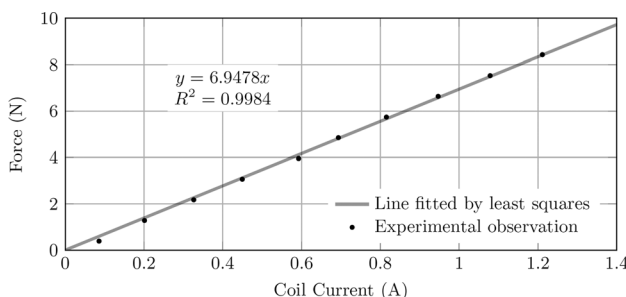


Fig. 5 Experimental results of the force constant testing

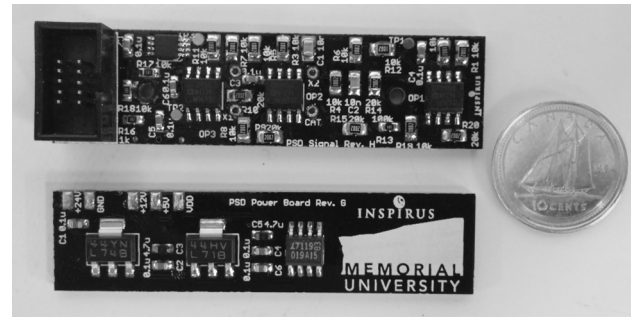


Fig. 6 Physical realization of the signal conditioning electronics

PSD was installed on the stator portion of the actuator, while the diode was integrated onto the PCB coil. To minimize the overall size of the actuator, the signal conditioning circuit and the electronics, which provide regulated power to the voice coil, were placed on separate circuits exhibited in Fig. 6. They are joined by way of multiple solder pads and held firmly in place by the body of the actuator.

As the active area of the chosen PSD is 12 mm and the analog-to-digital converter (ADC) included in the signal conditioning is 16 bit, the maximum theoretical resolution of the position is calculated to be approximately 0.1831 μm (i.e., 12 mm/($2^{16} - 1$)). The highly precise, feedback system was calibrated against a precision linear gauge (LGF 0125 L) with a resolution of 0.1 μm . For the experiment, the linear gauge provided the absolute position of the voice coil, whereas the signal conditioning circuit produced its discrete quantification of the position. The data were gathered at various coil positions and was fitted with a simple, linear regression model to produce a value of approximately 5.431 ADC counts per micron, exhibited in Fig. 7.

When a light spot is presented to the photosensitive surface of the PSD, two photocurrents are formed and driven through its two anodes, as shown in Fig. 8.

Due to the uniform resistivity of the active surface, the PSD acts as a current divider with the magnitudes of the generated currents dependent upon the exact location of the light spot within the active region. The exact point is calculated using the below equation [30]

$$x = \frac{L(I_2 - I_1)}{2(I_1 + I_2)} \quad (1)$$

Wherein x is the distance of the incident light from the center of the PSD, L is the length of the PSD's active area and I_1 and I_2 are the photocurrents through anodes one and two, respectively.

The calculation of Eq. (1) poses no real issue for a digital computer or other computation device. However, the division operation is generally computationally expensive and can limit the speed of an otherwise fast system. While additional analog

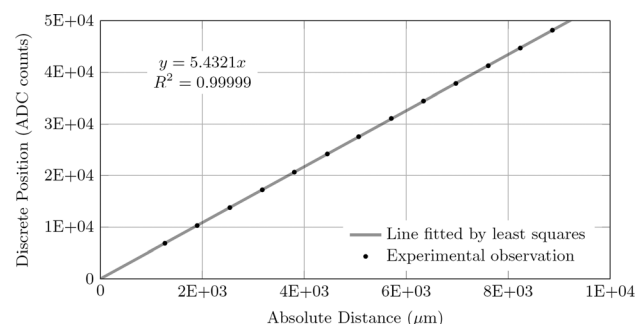


Fig. 7 Experimental calibration data for the PSD

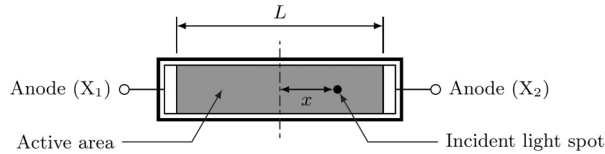


Fig. 8 Incident light detection of a PSD

electronics can solve this issue, they may introduce noise and negatively impact the quickness of the circuit. Since the sum of the photocurrents I_1 and I_2 are proportional to the quantity of light received by the PSD, it can be noted that keeping the incident light intensity consistent will in turn keep $I_1 + I_2$ constant. As shown in Eq. (2), this approach reduces Eq. (1) to a much simpler form, where L and the denominator are replaced by constant K , the gain determined by the calibration experiment. Thus, by adopting an integral control strategy for the power output of the VCSEL diode, $I_1 + I_2$ will remain constant, and Eq. (2) will hold true

$$x = k(I_2 - I_1) \quad (2)$$

Figure 9 illustrates a block diagram configuration of the overall signal conditioning circuit for the aforementioned PSD. The operation of the circuit begins as a light spot generates two photocurrents, I_1 and I_2 , as it strikes the active region of the PSD. These are swiftly converted to their corresponding voltages of V_1 and V_2 , by the current-to-voltage converters. The first order filter composition of these converters introduces a time constant of $100 \mu s$, which has been reduced by a factor of three in comparison to the $300 \mu s$ in the previous design. The two photocurrents, now represented as voltages, each enter a differential amplifier, thus computing their difference. This value is fed into the 16-bit ADC, essentially determining the position of the incident light spot hitting the PSD. As mentioned above, the sum of V_1 and V_2 is determined to ensure the power of the VCSEL diode remains constant by way of the integral control loop. Note, to guarantee the operational amplifiers (op-amps) and ADC do not impose a bottleneck on the speed of the circuit; an op-amp (OP295) having a slew rate of $0.03 V/\mu s$ and an ADC (ADS8325) with a high sampling rate of 100 kHz were chosen.

2.4 Guidance and Housing. The guidance and accurate linear alignment of the moving mass is a necessity when trying to achieve highly precise and dynamic actuation. These requirements were accomplished through the use of off-the-shelf ultra-miniature linear rails and ball-bearing carriages. They provide a smooth, almost frictionless displacement while still maintaining a low profile, allowing for the compact design of the VCA. Its physical realization is displayed in Fig. 10(a), followed by an exploded view of the actuator in Fig. 10(b).

The stator housing is composed of two similar sections allowing for the effortless insertion of the modified Halbach arrays. As

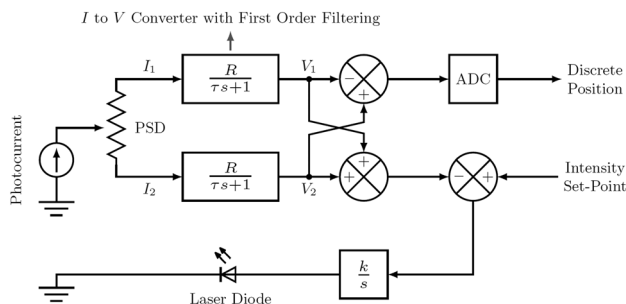


Fig. 9 Block diagram representation of the signal conditioning circuit

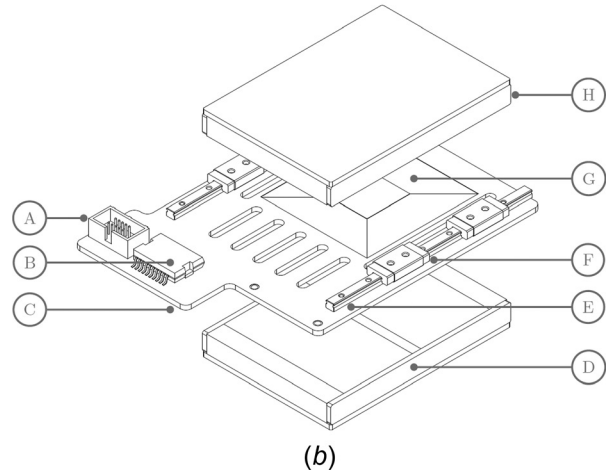
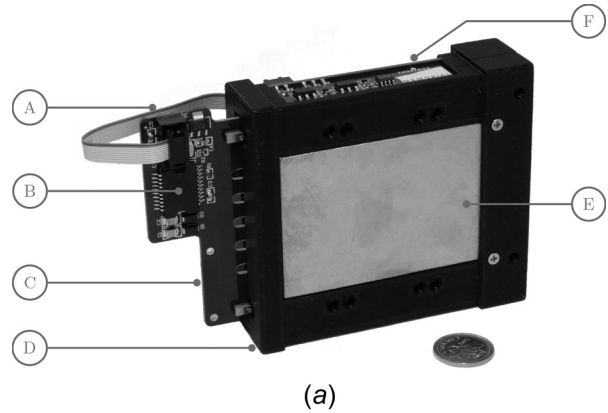


Fig. 10 Realization and exploded view of the novel VCA. (a) Physical prototype of the novel VCA: A—flexible ribbon cable for the transmission of power and data and control signals, B—drive electronics, C—voice coil PCB, D—magnet housing (VCA stator), E—modified Halbach array, and F—signal conditioning PCBs. (b) Exploded view of the VCA assembly: A—ribbon cable connector, B—H-bridge chip, C—voice coil PCB, D—bottom Halbach array, E—miniature linear bearing rail, F—linear bearing, G—coil traces, and H—top Halbach array.

well, it promotes simple fastening of the voice coil PCB, guidance mechanisms and is constructed for the incorporation of the PSD and signal conditioning circuits. To guarantee a lightweight, compact design, the housing for the actuator was manufactured out of PC-ABS using a fused deposition modeling (FDM) machine. The two sections are held in place due to the intense magnetic pull of the modified arrays. Also, to withstand this compression, pillars were introduced to the top section for additional reinforcement.

2.5 Experimentation and System Specifications. To validate the effect of the integral control circuit, an experimental study of both open loop (i.e., no control) and closed loop (i.e., integral control) responses of the PSD were completed over the full actuator stroke length. A dataset of 16 samples were recorded as a function of the actuator position in microns, versus the sum of the photocurrents in volts. For the open loop control, shown in Fig. 11(a), a constant current was supplied to the VSCSEL diode resulting in unfavorable fluctuations in the summation of the photocurrents. Conversely, Fig. 11(b) highlights how the current-controlled diode exhibits a much better performance with a minute variation of approximately $2 \mu V$.

To determine the open-loop performance of the VCA design, step inputs of three different magnitudes, 6 V , 12 V , and 24 V , were delivered to the drive electronics. The resulting motions of each input are recorded in Fig. 12. For each case, the moving

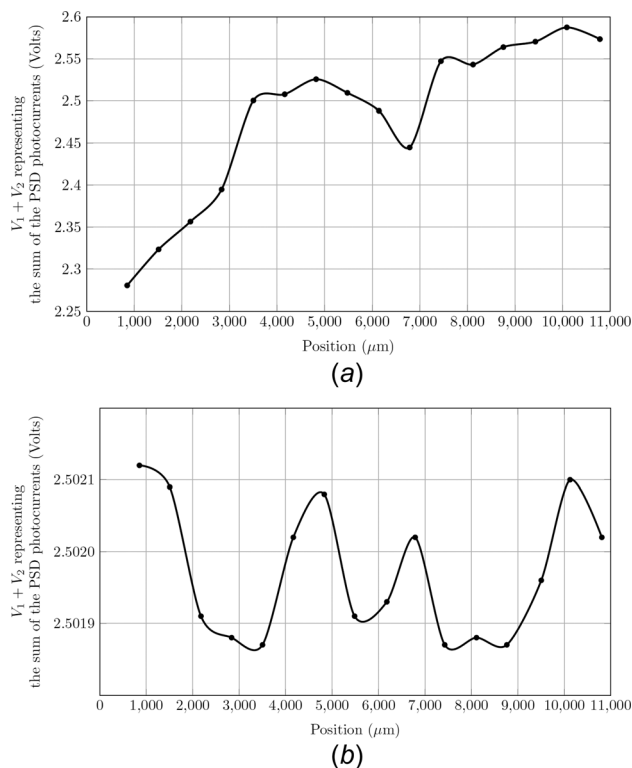


Fig. 11 Performance validation of the signal conditioning circuit integral control loop magnitudes: (a) summation of photocurrents without control and (b) summation of photocurrents with integral control

mass of the actuator accelerated against gravity. From the experimentation, it can be seen that maximum velocity of approximately 1.3 m/s was achieved while using a low-voltage power source.

From a theoretical perspective, if the VCA moves to a known discrete position multiple times, the absolute value should be consistent for each iteration. However, due to many factors such as thermal expansion, noise in the signal conditioning circuit, mechanical tolerances, and friction, this may not hold true. Therefore, it is essential to classify the VCA's repeatability characteristics. The variance, or standard deviation, in the absolute position can be used to categorize the repeatability. To determine this value, the coil assembly was secured to a coordinate measuring machine (CMM). The actuator was then moved to ten different positions, covering the stroke length of the coil. It was repeated five times in both up and down motion, resulting in 100 different points to consider. In its calibrated workspace, the CMM was used to locate the x , y , and z center points of the 1/4 in. spherical tooling ball attached to the actuator (Fig. 13). However, the z coordinate was only necessary since the motion of the coil was only in a linear manner. The experimental results are presented in Table 1.

Due to the limited resolution of the PSD, the VCA cannot be controlled to absolute perfection. Consequently, it does not come to rest at the exact discrete location for each experimental run. Therefore, the discrete position's standard deviation was logged to ensure it did not cause a poor repeatability in the actuator. Converting the deviation to an absolute value, it resulted in an extremely low maximum deviation of approximately 1.11 μm with its minimum being 0.22 μm . As indicated by the experimental outcome, even with the variation in the discrete position, the coil's repeatability is unprecedented, with the worst case scenario resulting in a standard deviation of 4.40 μm , with a 95% confidence interval range of $\pm 2.726 \mu\text{m}$.

During the initial stage of testing, it was deemed that the first set of data points were slightly higher, a maximum of

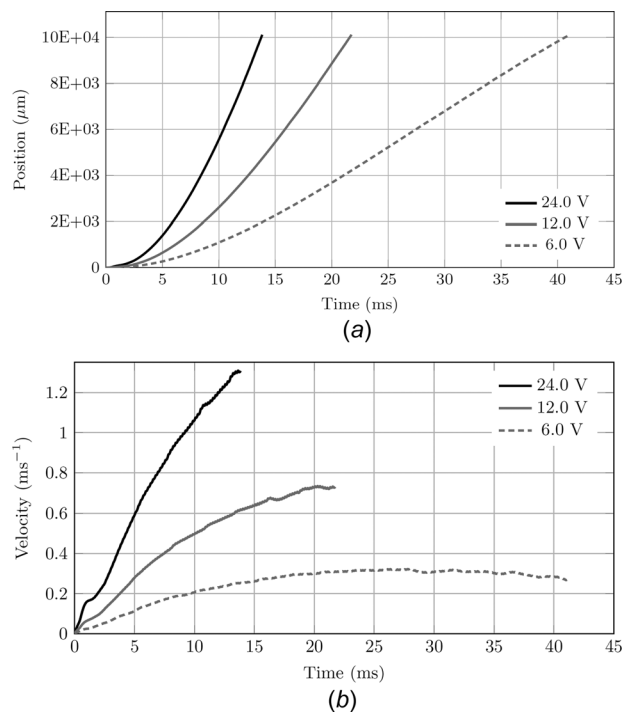


Fig. 12 Open loop responses of the VCA moving mass against gravity at varying magnitudes: (a) absolute response of the VCA and (b) velocity estimation of the VCA

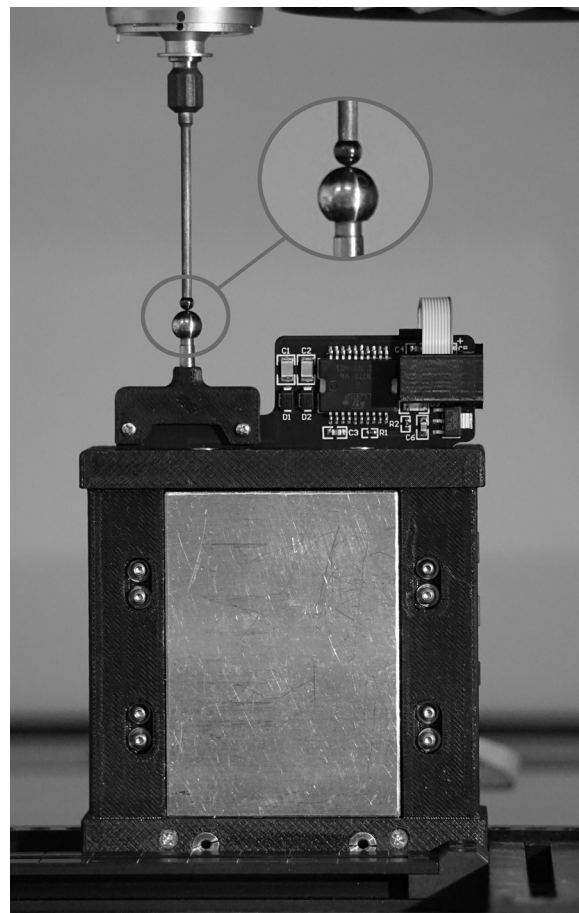


Fig. 13 VCA repeatability test experimental configuration

Table 1 VCA repeatability results

| Desired PSD value (ADC counts) | PSD SD (ADC counts) | PSD SD (μm) | Absolute position SD (μm) |
|-----------------------------------|------------------------|-----------------------------|---|
| 5000 | 4.69 | 0.86 | 4.40 |
| 11,111 | 4.77 | 0.88 | 3.91 |
| 17,222 | 5.90 | 1.09 | 4.18 |
| 23,333 | 5.89 | 1.08 | 3.67 |
| 29,444 | 6.03 | 1.11 | 4.11 |
| 35,556 | 5.51 | 1.01 | 3.14 |
| 41,667 | 5.12 | 0.94 | 2.51 |
| 47,778 | 3.74 | 0.69 | 3.27 |
| 53,889 | 2.15 | 0.40 | 2.75 |
| 60,000 | 1.18 | 0.22 | 3.05 |

approximately $2\mu\text{m}$, than the points of the subsequent tests. This was determined to be the consequence of a small quantity of thermal expansion as the PCB began to increase in temperature, from initially being at rest. Thus, additional testing was conducted to validate the repeatability at increased temperatures.

Given that the PCB is situated within the actuator assembly, it is difficult to heat through traditional means. Therefore, its temperature was increased by forcing the VCA to move to an unreachable position. This effectively supplied the coil with a high current until it achieved temperatures above 40°C . The tests were conducted in the same manner as the single VCA; however, prior to each movement, the actuator was reheated to ensure the temperature did not drop below 40°C . The experiment determined that average physical location of the moving mass is increased by approximately $29.8\mu\text{m}$ in comparison to the repeatability experiments.

These tests were completed twice to ensure there was not an error in the original data set and the results remained relatively the same as the second test showed an average increase of $30.4\mu\text{m}$. The variation is likely due to the thermal expansion of the PCB and the PC-ABS contained within the housing. Note, once the coil reaches a steady state temperature, the repeatability of the system remains on par with that of the initial experimentation.

Table 2 contains many of the key characteristics and parameters of the new iteration of the VCA. In order to validate the performance of the design, a comparison of the proposed actuator to VCAs in literature and industry was conducted. However, as previously indicated, it is difficult to compare the devices due to their many defining metrics. Nonetheless, it was determined that the system most resembling the discussed design was located in industry [14], as they share similar stroke lengths (i.e., 12 mm) and contain integrated guidance systems and position feedback devices. However, some contrasting features include the power requirements, force constant, size, and weight of each VCA. To elaborate, the industry device has a much lower total mass of 235 g, with a height of 72.8 mm, width of 56.6 mm, and depth of 20 mm, resulting in a smaller design compared with the values

Table 2 Novel VCA specifications

| Parameter | Value |
|-----------------------------|--------------------------|
| Height (fully retracted) | 113.97 mm |
| Stroke | 12 mm (nominal) |
| Width | 82.80 mm |
| Depth | 25.40 mm |
| Total mass | 520 g |
| Moving mass | 33 g |
| Force constant | 6.9478 N/A |
| Back EMF constant | 6.9478 V s/m |
| Static friction coefficient | 0.500 |
| Magnetic flux density | 0.704 T (typical) |
| Coil resistance | 20.44 Ω (typical) |
| Coil inductance | 1.27 mH (typical) |

contained in Table 2. In contrast, the proposed design requires less voltage, 24 V compared to 48 V, while generating a larger force constant, 6.95 N/A opposed to 3.6 N/A, while containing a moving mass of 33 g in comparison to 40 g of the commercial actuator. Additionally, the compared actuator requires multiple connections and power sources to function, while the presented VCA needs a simple 10-pin connector and single 24 V input. Furthermore, the drive electronics are integrated in the discussed architecture, while absent from the industry mechanism. This is important, as it leaves the task of configuring such circuitry up to the end user. Finally, while a direct comparison of all metrics is not achievable, these parameters act as an indication of the proposed actuator's validity.

3 Parallel Orientation Manipulators: Applications of the Novel Voice Coil

Parallel kinematic mechanisms are an assembly of links where a payload or mobile platform is supported by multiple kinematic chains so that the payload is capable of possessing some desired motion patterns. The platform experiences a number of DOF proportional to the number of nonredundant actuators used in its design. When referring to PKMs, which solely involve rotational motion, they can be more specifically referred to as a POM.

POMs have existed in industry for many years and are used in a vast selection of applications; in particular, systems utilized for optomechatronic purposes such as visual tracking, sense and avoidance, active vision, and vibration isolation [31,32]. However, when designing miniature POMs, the necessary actuators must be highly responsive and extremely accurate. Unfortunately, commercially available linear motors often fall short of delivering these requirements. However, the novel voice coil, due to its aforementioned parameters, is an optimal fit for use with these POMs. Therefore, to exploit the VCA's speed and precision, two distinct POM designs were pursued: one exhibiting 3DOF and the other 2DOF, each of which has its advantages. As this paper is concentrated on the development and specifications of the novel voice coil, only a brief description and few defining parameters of each POM will be discussed. For a more thorough examination of each of these configurations, refer to Rahman [33].

3.1 POM Architectures. There are an abundant number of configurations which can produce a 3DOF POM [34–36]. Nevertheless, after considering the POM's potential optomechatronic applications, the 3-PSS/S was chosen as the desired architecture due to its compact design. In this case, P and S refer to the prismatic (linear) and spherical motions of the joints, respectively.

The kinematic structure, or truss model, and its CAD representation shown in Fig. 14 showcases this configuration with each of its joints labeled in increments of A, B, C, or O. The limbs A_iB_i represent the actuated prismatic joints while B_iC_i are intermediate links connecting the linear actuators to the moving platform defined by $C_1C_2C_3$. This platform is attached to spherical joint O, which restricts the moving platform to rotation only resulting in tilt, azimuth, and torsion angular motion. However, torsional rotation is not essential in many applications, especially those when the payload of the moving platform is axis symmetric, such as a laser device. Therefore, a torsion restricted, 2DOF POM was researched to minimize the number of actuators and thus reduce the weight, cost, and power requirements of the mechanism.

Since a torsion restricted POM requires a reduced number of actuators, it can be stated that the architecture of the system is less complex than that of the 3DOF mechanism. Though there are many examples of 2DOF orientation manipulators [23,37–39], the 2-PSS/U, U corresponding to a universal joint, arrangement was ultimately chosen as it most closely resembles the 3-PSS/S. Similar to the 3DOF mechanism, the kinematic representation of the torsion restriction variant is shown in Fig. 15. Similarly, links A_iB_i correspond to the limbs capable of linear actuation, whereas

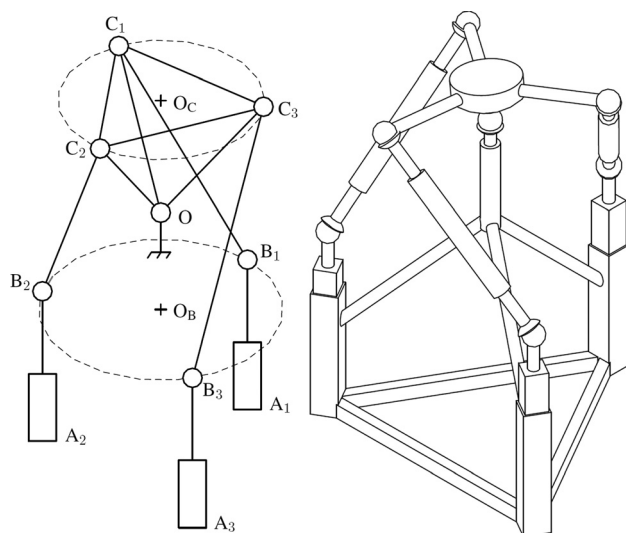


Fig. 14 3-PSS/S kinematic structure (left) and CAD representation (right)

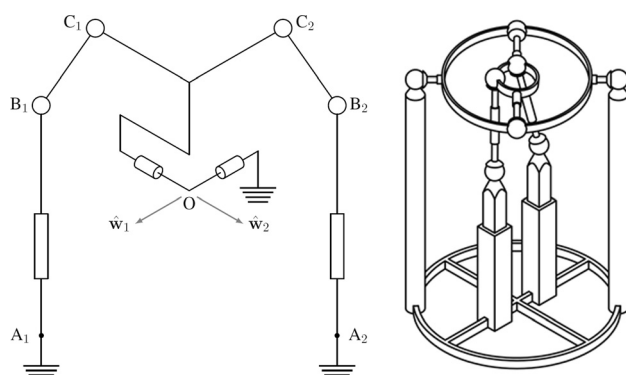


Fig. 15 2-PSS/U kinematic structure (left) and CAD representation (right)

spherical joints B_i and C_i form the link between the prismatic joints and mobile platform, defined by link C_1C_2 . Conversely, the universal joint has been reconfigured into two revolute joints, \hat{w}_1 and \hat{w}_2 . These axes are perpendicular to one another intersect at point O.

While the 3DOF model closely resembles that of the kinematic structure, the 2DOF varies greatly as the revolute joints are designed to be ring like in nature due to its geometry. This design promotes a less coupled system than the 3DOF, resulting in an almost one-to-one relationship with respect to actuator movement and the tilt and azimuth angles.

Before prototyping, well-defined 3D models of both of the POM were implemented using CAD software to provide early visualization of the systems, as well as perform preliminary testing. The final CAD model revisions and their physical realization are shown in Figs. 16 and 17. Finally, upon the realization of both structures, they were utilized in a number of optomechatronic applications throughout the broad scope of the research. These include object tracking and targeting, laser pointing and free space optical communication.

3.2 POM Experimentation and System Specifications.

While there are many parameters to compare and contrast between the two systems, a few key specifications were chosen to highlight some of the major differences. The first, as seen in Fig. 18, is the workspace obtained by the moving platform of the 3DOF and 2DOF.

A POM's reachable workspace is the set of orientations of which the moving platform can realize without violating any physical constraint (e.g., motion range of the joints, interference of links, etc.), whereas the regular workspace of a POM is defined by the maximal geometric object (e.g., cube, sphere, etc.) that can be completely contained within the reachable workspace [40]. This is more often used to evaluate the angular range of a mobile platform. Each of the architectures perform very well; however, the 3DOF mechanism achieved a slightly better angular workspace proving a maximum angular tilt of 32 deg as opposed to the 26 deg of the 2DOF.

Another key element is the repeatability of the system, which now encompasses not only the potential error in the voice coil but also any misalignment, tolerances, and manufacturing issues involving the kinematic links and the moving platform. The tests were accomplished in similar fashion to the single actuator testing with examples of the testing apparatus shown in Fig. 19.

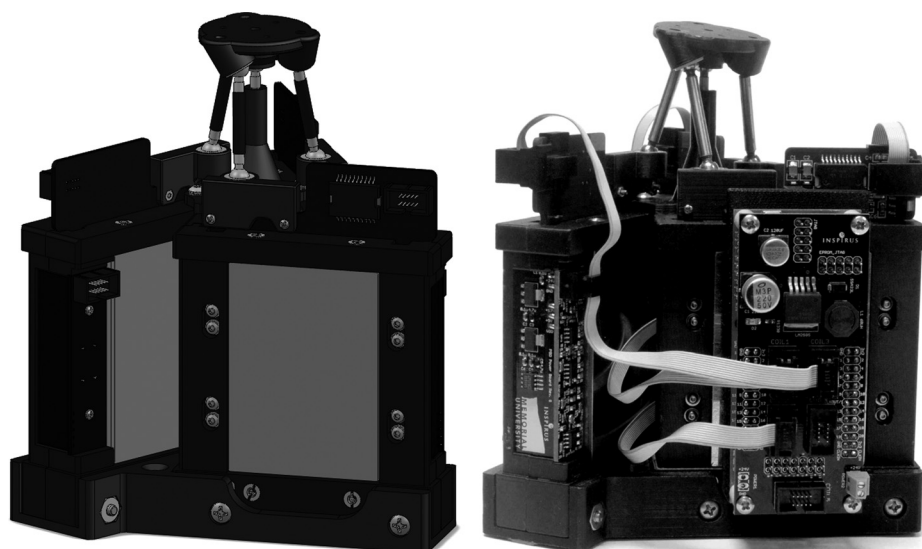


Fig. 16 CAD Model (left) and physical realization (right) of the 3DOF POM

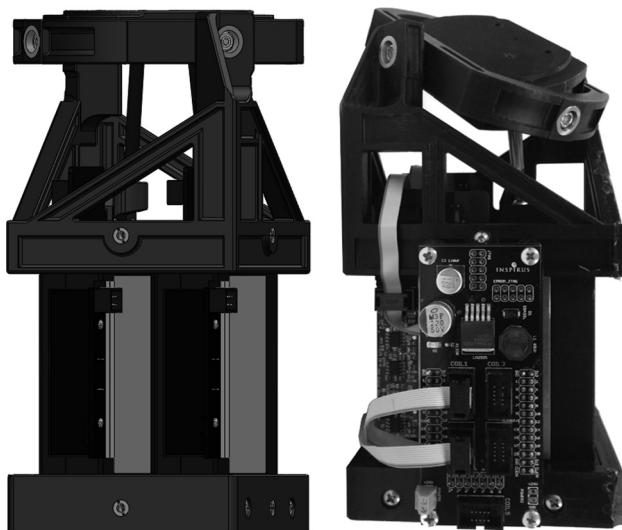


Fig. 17 CAD Model (left) and physical realization (right) of the 2DOF POM

To define an orientation in 3D space, a minimum of three points are required; thus, a mobile platform containing an additional two balls was attached to each POM. For the experiments, both POMs were moved to ten unique positions and repeated five times in order to create a varied data set. From this, nine measurements were evaluated by the CMM (the x , y , and z coordinates of each ball) at each position and the standard deviation of each was calculated. As a result, the average and maximum standard deviations for the 50 movements were calculated to be approximately $10.9\text{ }\mu\text{m}$ and $35.4\text{ }\mu\text{m}$ for the 3DOF system, while the 2DOF outcomes were poorer at $31.1\text{ }\mu\text{m}$ and $76.7\text{ }\mu\text{m}$. The deviation in the repeatability of the POMs is likely due to the aforementioned tolerance issues while prototyping the device as the 2DOFs end effector contains more prototyped parts. These values are higher than the reported $3.5\text{ }\mu\text{m}$ of the single coil, but still are quite impressive, especially for rapid-prototyped mechanisms with many interconnecting links.

Table 3 denotes the dimensions of each of the POMs. As shown, the height of the 2DOF is larger in comparison with the 3DOF due to the size of its end effector. However, as it contains less linear actuators, the width, depth, and weight have been reduced significantly. This is extremely important when dealing with many optomechatronic applications as generally they have

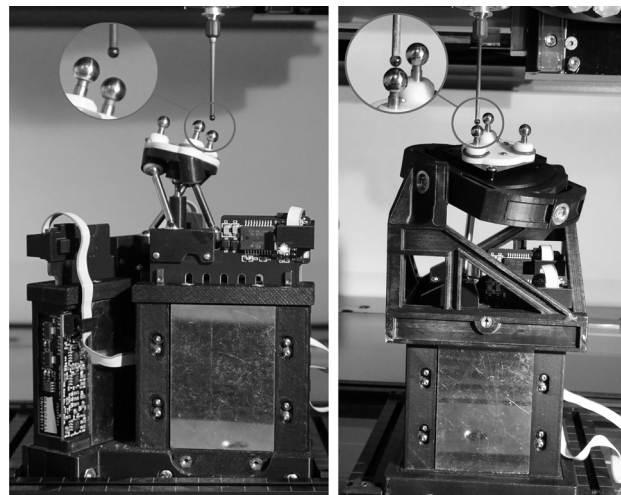


Fig. 19 Three degrees-of-freedom (left) and 2DOF (right) POM repeatability experimental configurations

Table 3 3DOF and 2DOF POM specifications

| Parameter | 3DOF | 2DOF |
|-------------------------------|-------|-------|
| Width (mm) | 136.7 | 97.3 |
| Depth (mm) | 136.7 | 79.8 |
| Height (mm) | 147.7 | 175.5 |
| Weight (kg) | 1.71 | 1.27 |
| Max angle (deg) | 32 | 26 |
| Typical Azimuth speed (deg/s) | 1500 | 1000 |
| Typical tilt speed (deg/s) | 1500 | 800 |
| Typical torsion speed (deg/s) | 1000 | — |

strict SWaP requirements. Also, due to the removable of one actuator, its dynamics was negatively affected, reducing the speed of the 2DOF mechanism. Finally, as the two structures exhibit different constraints (i.e., size, force, etc.), the ideal mechanism cannot be chosen outright as an application must first be identified.

4 Conclusions

With optomechatronic applications in mind, a uniquely designed, highly dynamic novel voice coil actuator has been created. The

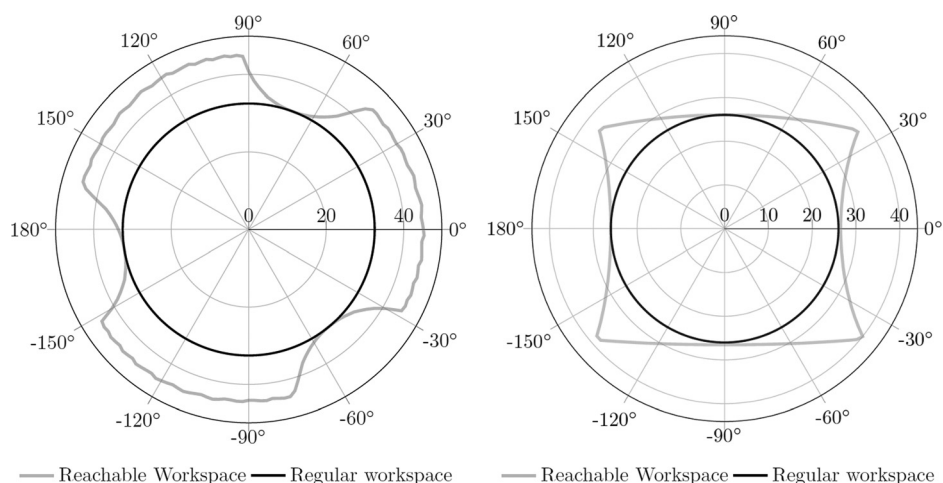


Fig. 18 Reachable and regular workspaces of the 3DOF (left) and 2DOF (right) POMs. Radial axis: tilt angle and angular axis: azimuth angle.

redesigned VCA package is very lightweight and compact in comparison to traditional, off-the-shelf models while still incorporating a miniature guidance system and high-resolution positioning electronics. These combine to provide a VCA with low friction capabilities, a static friction coefficient of 0.500, extreme precision of less than $0.2\text{ }\mu\text{m}$ with positioning repeatability of $\pm 2.726\text{ }\mu\text{m}$ within a 95% confidence interval. Furthermore, the highly integrated coil is now capable of producing an impressive force constant of approximately 7 N/A with peak velocities in excess of 1.3 m/s and accelerations surpassing 30 g . Utilizing the high performance of the actuator, 3-PSS/S and 2-PSS/U configured POMs were developed in the pursuit of optomechatronic applications. Both of these devices are capable of highly dynamic, precise orientation of a mobile platform and any device attached to it. Due to these specifications, numerous uses such as sense and avoidance of unmanned aerial vehicles, accurate pointing devices, and active vision systems are achievable.

Acknowledgment

The authors would like to thank Tom Pike, Brian Pretty, Steve Steele, and Don Taylor for their valuable advice and technical expertise during the design and testing of the actuator. The authors also thank the Atlantic Canada Opportunities Agency (ACOA), the Research and Development Corporation of Newfoundland and Labrador (RDCNL), Boeing and all other sources of funding for the Inspirit project.

References

- [1] Baronti, F., Lazzeri, A., Lenzi, F., Roncella, R., Salletti, R., and Saponara, S., 2009, "Voice Coil Actuators: From Model and Simulation to Automotive Application," 35th Annual Conference of IEEE Industrial Electronics (IECON), Porto, Portugal, Nov. 3–5, pp. 1805–1810.
- [2] Feng, X., Duan, Z., Fu, Y., Sun, A., and Zhang, D., 2011, "The Technology and Application of Voice Coil Actuator," 2nd International Conference on Mechanism Automation and Control Engineering (MACE), Hohhot, China, July 15–17, pp. 892–895.
- [3] Remy, M., Lemarquand, G., Castagnede, B., and Guyader, G., 2008, "Ironless and Leakage Free Voice-Coil Motor Made of Bonded Magnets," *IEEE Trans. Magn.*, **44**(11), pp. 4289–4292.
- [4] Vrijns, N., Jansen, J., and Lomonova, E., 2010, "Comparison of Linear Voice Coil and Reluctance Actuators for High-Precision Applications," 14th International Power Electronics and Motion Control Conference (EPE/PEMC), Ohrid, Macedonia, Sept. 6–8, pp. 23–29.
- [5] Moticont, 2016, "Linear Voice Coil Motors," Moticont, Van Nuys, CA, accessed June 18, 2016, <http://www.moticont.com/voice-coil-motor.htm>
- [6] BEI Kimco, 2016, "Linear Voice Coil Actuators (VCA)," BEI Kimco Ltd., Vista, CA, accessed June 16, 2016, <http://www.beikimco.com/motor-products/VCA-linear-voice-coil-actuator-all>
- [7] McBean, J., and Breazeal, C., 2004, "Voice Coil Actuators for Human-Robot Interaction," IEEE/RSJ International Conference on Intelligent Robots and Systems (IROS), Sendai, Japan, Sept. 28–Oct. 2, pp. 852–858.
- [8] Ruddy, B. P., Hunter, I. W., and Taberner, A. J., 2014, "Optimal Voice Coil Actuators for Needle-Free Jet Injection," 36th Annual International Conference of the IEEE Engineering in Medicine and Biology Society (EMBC), Chicago, IL, Aug. 26–30, pp. 2144–2148.
- [9] Janssen, J., Paulides, J., and Lomonova, E., 2011, "Design of an Ironless Voice Coil Actuator With a Rectangular Coil and Quasi-Halbach Magnetization," XV International Symposium on Electromagnetic Fields (ISEF), Funchal, Madeira, Sept. 1–3, pp. 1–8.
- [10] Li, L., Pan, D., Tang, Y., and Wang, T., 2011, "Analysis of Flat Voice Coil Motor for Precision Positioning System," International Conference on Electrical Machines and Systems (ICEMS), Beijing, China, Aug. 20–23, pp. 1–4.
- [11] Akribis Systems, 2016, "AVA Voice Coil," Akribis Systems Pte Ltd., San Jose, CA, accessed June 18, 2016, <http://www.akribis-sys.com/Details.aspx?ID=14>
- [12] Moticont, 2016, "Linear Motor Actuators," Moticont, Van Nuys, CA, accessed June 18, 2016, <http://www.moticont.com/linear-motor-actuator.htm>
- [13] BEI Kimco, 2016, "Rectangular Linear Voice Coil Actuators (VCA)," BEI Kimco Ltd., Vista, CA, accessed June 16, 2016, <http://www.beikimco.com/motor-products/VCA-linear-voice-coil-actuator-all/rectangularl>
- [14] PBA Systems, 2014, "Rectangular Voice Coil Actuator—RVCA," PBA Systems Pte Ltd., Singapore, accessed June 14, 2016, <http://www.pbasystems.com.sg/products/voice-coil-modules/rvca-rectangular-voice-coil-actuator.html#lm-specifications>
- [15] Halbach, K., 1980, "Design of Permanent Multipole Magnets With Oriented Rare Earth Cobalt Material," *Nucl. Instrum. Methods*, **169**(1), pp. 1–10.
- [16] Binnard, M. B., Gery, J.-M., and Hazelton, A. J., 2008, "High Efficiency Voice Coil Motor," U.S. Patent No. **7,368,838**.
- [17] Narayanan, C., Buckman, A. B., and Busch-Vishniac, I., 1997, "Noise Analysis for Position-Sensitive Detectors," *IEEE Trans. Instrum. Meas.*, **46**(5), pp. 1137–1144.
- [18] Kong, X., Yu, J., and Li, D., 2016, "Reconfiguration Analysis of a Two Degrees-of-Freedom 3-4R Parallel Manipulator With Planar Base and Platform," *ASME J. Mech. Rob.*, **8**(1), p. 011019.
- [19] Wang, J., and Gosselin, C. M., 2004, "Singularity Loci of a Special Class of Spherical 3-DOF Parallel Mechanisms With Prismatic Actuators," *ASME J. Mech. Des.*, **126**(2), pp. 319–326.
- [20] Nurahmi, L., Schadlbauer, J., Caro, S., Husty, M., and Wenger, P., 2015, "Kinematic Analysis of the 3-RPS Cube Parallel Manipulator," *ASME J. Mech. Rob.*, **7**(1), p. 011008.
- [21] Bonev, I. A., and Gosselin, C. M., 2005, "Singularity Loci of Spherical Parallel Mechanisms," IEEE International Conference on Robotics and Automation (ICRA), Barcelona, Spain, Apr. 18–22, p. 2957.
- [22] Villgratner, T., and Ulbrich, H., 2010, "Optimization and Dynamic Simulation of a Parallel Three Degree-of-Freedom Camera Orientation System," IEEE/RSJ International Conference on Intelligent Robots and Systems (IROS), Taipei, Taiwan, Oct. 18–22, pp. 2829–2836.
- [23] Villgratner, T., and Ulbrich, H., 2011, "Design and Control of a Compact High-Dynamic Camera-Orientation System," *IEEE/ASME Trans. Mechatronics*, **16**(2), pp. 221–231.
- [24] Ma, J., Yang, T., Hou, Z.-G., and Tan, M., 2009, "Neural Network Disturbance Observer Based Controller of an Electrically Driven Stewart Platform Using Backstepping for Active Vibration Isolation," International Joint Conference on Neural Networks, (IJCNN), Atlanta, GA, June 14–19, pp. 1939–1944.
- [25] Tahri, O., Mezouar, Y., Andreff, N., and Martinet, P., 2009, "Omnidirectional Visual-Servo of a Gough-Stewart Platform," *IEEE Trans. Rob.*, **25**(1), pp. 178–183.
- [26] Choi, J.-K., Lee, H.-I., Yoo, S.-Y., and Noh, M. D., 2012, "Analysis and Modeling of a Voice-Coil Linear Vibration Motor Using the Method of Images," *IEEE Trans. Magn.*, **48**(11), pp. 4164–4167.
- [27] Robertson, W., Cazzolato, B., and Zander, A., 2010, "Parameters for Optimizing the Forces Between Linear Multipole Magnet Arrays," *IEEE Magn. Lett.*, **1**, p. 0500304.
- [28] Wang, J., Li, C., Li, Y., and Yan, L., 2008, "Optimization Design of Linear Halbach Array," International Conference on Electrical Machines and Systems (ICEMS), Wuhan, China, Oct. 17–20, pp. 170–174.
- [29] Krouglicof, N., Morgan, M., Pansare, N., Rahman, T., and Hicks, D., 2013, "Development of a Novel PCB-Based Voice Coil Actuator for Opto-Mechatronic Applications," IEEE/RSJ International Conference on Intelligent Robots and Systems (IROS), Tokyo, Japan, Nov. 3–7, pp. 5834–5840.
- [30] Hamamatsu Photonics, 2011, "One-Dimensional PSD S3931, S3932, S3270," White Paper, Hamamatsu Photonics K. K., Hamamatsu City, Japan, accessed June 12, 2016, https://www.hamamatsu.com/resources/pdf/ssd/s3931_etc_kpsd1002e.pdf
- [31] Fatehi, M., Vali, A., Eghesad, M., Fatehi, A., and Zarei, J., 2011, "Kinematic Analysis of 3-PRS Parallel Robot for Using in Satellites Tracking System," Second International Conference on Control, Instrumentation and Automation (ICCIA), Shiraz, Iran, Dec. 27–29, pp. 929–934.
- [32] Villgratner, T., and Ulbrich, H., 2008, "Piezo-Driven Two-Degree-of-Freedom Camera Orientation System," IEEE International Conference on Industrial Technology (ICIT), Chengdu, China, Apr. 21–24, pp. 1–6.
- [33] Rahman, T., 2015, "Design Synthesis and Prototype Implementation of Parallel Orientation Manipulators for Optomechatronic Applications," Ph.D. thesis, Memorial University of Newfoundland and Labrador, St. John's, NL, Canada.
- [34] Fang, Y., and Tsai, L.-W., 2002, "Structure Synthesis of a Class of 4-DOF and 5-DOF Parallel Manipulators With Identical Limb Structures," *Int. J. Rob. Res.*, **21**(9), pp. 799–810.
- [35] Gallardo-Alvarado, J., García-Murillo, M., and Pérez-González, L., 2013, "Kinematics of the 3RRRS+S Parallel Wrist: A Parallel Manipulator Free of Intersecting Revolute Axes#," *Mech. Based Des. Struct. Mach.*, **41**(4), pp. 452–467.
- [36] Di Gregorio, R., 2004, "Kinematics of the 3-RSR Wrist," *IEEE Trans. Rob.*, **20**(4), pp. 750–753.
- [37] Stan, S.-D., Maties, V., and Balan, R., 2007, "Genetic Algorithms Multiobjective Optimization of a 2 DOF Micro Parallel Robot," International Conference on Emerging Technologies and Factory Automation (ETFA), Patras, Greece, Sept. 25–28, pp. 522–527.
- [38] Adelstein, B. D., and Rosen, M. J., 1992, *Design and Implementation of a Force Reflecting Manipulandum for Manual Control Research*, Vol. 42, ASME, New York, pp. 1–12.
- [39] Palpacelli, M.-C., Palmieri, G., and Callegari, M., 2012, "A Redundantly Actuated 2-Degrees-of-Freedom Mini Pointing Device," *ASME J. Mech. Rob.*, **4**(3), p. 031012.
- [40] Lou, Y., Liu, G., Chen, N., and Li, Z., 2005, "Optimal Design of Parallel Manipulators for Maximum Effective Regular Workspace," IEEE/RSJ International Conference on Intelligent Robots and Systems (IROS), Edmonton, AB, Canada, Aug. 2–6, pp. 795–800.